Journal of Fluids and Structures 43 (2013) 385–401

Contents lists available at ScienceDirect

Journal of Fluids and Structures

journal homepage: www.elsevier.com/locate/jfs

Fluttering flags: An experimental study of fluid forces

Emmanuel Virot [a,*], Xavier Amandolese [a,b], Pascal Hémon [a]

[a] Laboratoire d'Hydrodynamique (LadHyX), CNRS UMR 7646, École Polytechnique, 91128 Palaiseau, France
[b] Département ISME, Conservatoire National des Arts et Métiers - 75003 Paris, France

ARTICLE INFO

Article history:
Received 25 April 2013
Accepted 3 September 2013
Available online 17 October 2013

Keywords:
Flutter
Flag
Unsteady forces
Drag
Wind tunnel

ABSTRACT

Unsteady fluid forces are measured at the onset of flutter and during the post-critical flutter of flags placed in a wind tunnel, focusing on the drag force and the moment around the flagpole. The evolution of these forces during flutter mode switches, induced by varying either the mass ratio or the wind velocity, is discussed by using additional high-speed imaging. For the highest wind velocities, losses of periodicity and snapping events are reported. Time-averaged and unsteady drag coefficients are reported and compared to previous works.

1. Introduction

In the early 1930s, the need to design airplanes towing advertising banners led Fairthorne to study the drag of flags and more particularly the additional drag due to flutter (Fairthorne, 1930). In a wind tunnel, he measured drag coefficients for many cloth flags and he provided empirical formulas. This pioneering work led to the curious conclusion that the longer the flag, the smaller the drag. Later, Hoerner recovered Fairthorne's data and stressed the fact that fluttering flags had an additional time-averaged drag 10 times higher than the skin friction drag (Hoerner, 1965). Taneda (1968) confirmed this huge increase of drag with a broader range of materials.

Interestingly, these works gave rise to innovative decelerators based on flutter-induced drag force, such as elementary parachutes on falling bodies (Lokerson, 1968). Similarly, observations of sailors removing veil flutter to speed up their race suggested to use flags for improving vehicles braking (Bourrières, 1969). Flags were also studied for stabilizing the rotary motion of projectiles (Fancett and Clayden, 1972) or for preventing side-impact of rockets (Auman and Wilks, 2005).

Time-averaged drag coefficients of fluttering flags can be found in a few recent publications (see Carruthers and Filippone, 2005; Wilk and Skuta, 2009; Morris-Thomas and Steen, 2009). A simple model was suggested by Moretti (2003), who extended the works of Thoma (1939a,b) to estimate time-averaged tension at the flagpole from the loss of kinetic energy at the trailing edge of flags. This elementary model was confirmed by experiments on heavy flags in a wind tunnel (Martin, 2006). A fresh look on the time-averaged drag of flags was recently offered by Ristroph and Zhang (2008) with the configuration of tandem flags: the leading flag suffers from less drag than the downstream flag, i.e. the opposite of the intuitive steady drafting situation (see also the subsequent works of Alben, 2009; Zhu, 2009; Kim et al., 2010).

In practice, the use of time-averaged drag coefficients hides the profound nature of instantaneous drag which varies with time and which – above all – is not necessarily periodic. A striking example is given by snapping events (irregular and violent accelerations) which are predicted above the threshold of instability (see Connell and Yue, 2007; Alben and Shelley, 2008; Michelin et al., 2008). However, we did not find experimental studies on unsteady forces acting on a flagpole, despite numerous

* Corresponding author. Tel.: +33 1 69 33 52 86.
E-mail address: emmanuel.virot@ladhyx.polytechnique.fr (E. Virot).

0889-9746/$ - see front matter © 2013 Elsevier Ltd. All rights reserved.
http://dx.doi.org/10.1016/j.jfluidstructs.2013.09.012

and leading applications. This is the strongest motivation of the present paper, the other motivations being to report new visualizations of flutter mode switches and new evidences of loss of periodicity and snapping events above the threshold of instability.

The flag flutter motivated many theoretical works as well, most of them starting from a note of Lord Rayleigh on liquid jets destabilization: "[…] Its bearing upon the flapping of sails and flags will be evident. […]" (Lord Rayleigh, 1878). The modeling of flag flutter above the threshold of instability is still in progress to provide a complete picture of flag dynamics (see Païdoussis, 2004; Shelley and Zhang, 2011, for recent reviews on flag models). Flag models also promise excellent perspectives for wind energy harvesting (see Tang et al., 2009; Doaré and Michelin, 2011; Dunnmon et al., 2011; Michelin and Doaré, 2013), and some models are specifically designed for predicting flutter-induced forces on the flagpole (see Connell and Yue, 2007; Alben and Shelley, 2008; Michelin et al., 2008). In this context as well, it was necessary to have an experimental background for flutter-induced forces on the flagpole.

The present paper is organized as follows: experimental techniques are introduced in Section 2; the onset of flutter is studied in Section 3, where unsteady forces acting on the flagpole are discussed when the flag length is varied; the flutter beyond boundary of instability is addressed in Section 4, where unsteady forces acting on the flagpole are discussed when the wind velocity increases. In Section 5, we discuss the relative importance of unsteady drag to time-averaged drag. A summary of the findings is provided in Section 6.

2. Experimental techniques

In this section, we first present geometric parameters and material properties of flags, then the wind tunnel is briefly described and the force measurement system is detailed. We conclude by explaining the measurement process with an example.

2.1. Flags

Rectangular flags are cut in the 29.7 cm direction of A4 sheets of paper (Clairalfa 120 g/m^2), which is the principal fiber direction. These flags have a thickness $d = 150$ μm and a mass density $\rho_p = 790$ kg/m^3. The flag length (chord) is varied in the range $L = 70$–290 mm. The flag width (span) is unchanged: $H = 100$ mm. The width-to-length ratio $H^* = H/L$ is thus varied in the range $H^* = 0.3$–1.4.

A usual method for determining elastic properties of a material is to measure Young's modulus (E) by a tensile test (see Watanabe et al., 2002b). As shown in Fig. 1(a), a tensile test assesses the validity of the elastic deformation hypothesis (tensile stress $\leq$ yield stress) and gives a tear criterion (tensile stress $=$ ultimate strength). We measured $E = 3.3 \pm 0.2$ GPa (mean value $\pm$ standard deviation on four tests). This value is consistent with common Young's modulus of paper in the principal fiber direction (see Yamaguchi et al., 2000b; Alava and Niskanen, 2006).

However, this method gives only an ideal (under)estimation of the flexural rigidity $\mathcal{D} = Ed^3/12(1-\nu^2)$, where d is the flag thickness and ν is Poisson's ratio. Indeed, the flag suffers from unavoidable flatness defects (curvature) at the flagpole fixation. Since flatness defects are large compared to flag thickness, they have a significant influence on the onset of flutter, as recently shown in Eloy et al. (2012). Accordingly, we decided to measure an effective flexural rigidity, taking into account the flagpole fixation. The effective flexural rigidity can be measured on vertical paper sheets standing vertically on a fixation similar to the flagpole fixation (see Lemaitre et al., 2005). Then, the method is based on the critical sheet length (L_b) above which Euler's buckling occurs: this is illustrated in Fig. 1(b). Several tests were performed for compensating uncertainty. We finally deduced the flexural rigidity from $\mathcal{D} \simeq 0.13\rho_p g d L_b^3$, where ρ_p is the paper mass density, g the gravity acceleration and d the flag thickness (Timoshenko and Gere, 1963). Flags have a buckling length $L_b = 226 \pm 16$ mm and thus we obtain $\mathcal{D} = 1.7 \pm 0.2$ mN m (mean value $\pm$ standard deviation on 72 tests). This value of flexural rigidity is associated with an effective Young's modulus $E = 5.9 \pm 0.7$ GPa far greater than the previous estimation. This effective flexural rigidity will be used in the present work for nondimensionalization. Note that flatness defects are probably removed during flutter due to

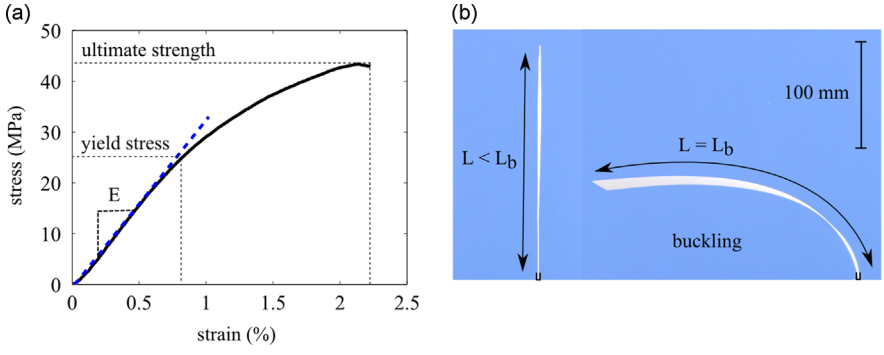

Fig. 1. Elastic properties of the flag material (paper): (a) stress–strain curve obtained from a tensile test in the longitudinal direction of the flag; (b) measurement of the buckling length.

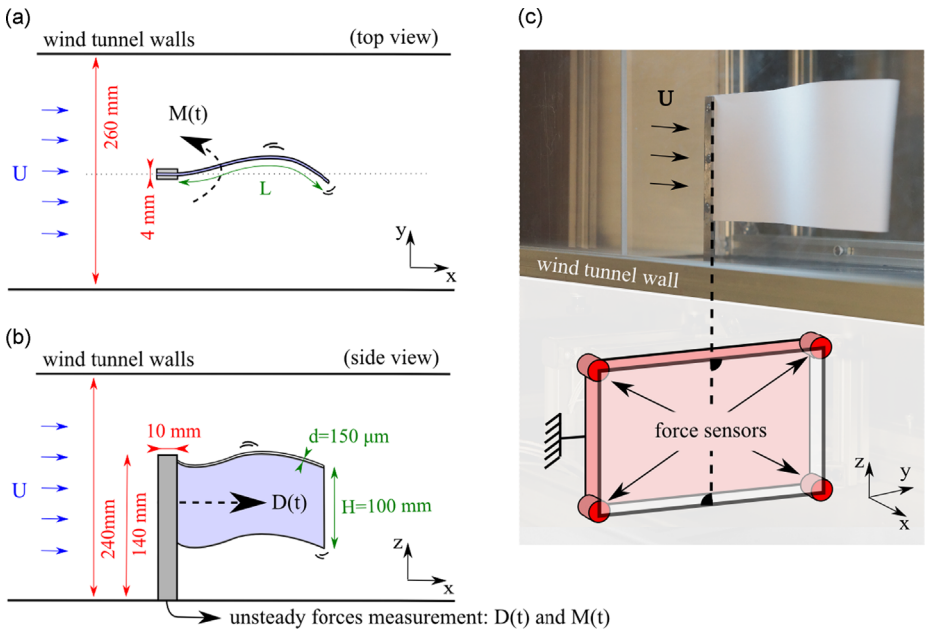

Fig. 2. Wind tunnel characteristics: (a) top view of the wind tunnel, containing a fluttering flag fixed on its flagpole; (b) side view; (c) snapshot of a flag of length $L = 200$ mm fluttering in the wind tunnel at a wind velocity $U = 12$ m/s; outside the wind tunnel the force measurement system is designed with four piezoelectric force sensors connected to the flagpole.

the energetic cost of having a non-zero Gauss curvature (Eloy et al., 2012). The flattening during flutter is however difficult to confirm experimentally because the characteristic length scale is essentially the flag thickness ($\sim 100\ \mu$m).

2.2. Wind tunnel

The flag is placed in an Eiffel-type wind tunnel with a rectangular test-section: width $\times$ height $= 260$ mm $\times$ 240 mm. Several views of this set-up are offered in Fig. 2. The flag is clamped inside a flagpole of thickness 4 mm and height 140 mm. Tests are performed for a wind velocity varying from 3 to 18 m/s, and the turbulence level – the relative importance of velocity fluctuations in the wind tunnel – is approximately 0.4% over this velocity range. Accordingly, the Reynolds number based on the flag length (L) falls in the range $\mathrm{Re}_L = 1.4 \times 10^4$–$3.4 \times 10^5$. Due to the bluff rectangular section of the flagpole, the boundary layer all along the flag is probably turbulent in our experiments. A high-speed video camera VDS Vosskühler HCC1000 records the flag motion from the top of this wind tunnel. It captures 462 frames per second (exposure time $= 2.16$ ms) with a resolution of 1024×1024 pixels. In practice, this is sufficient to observe approximately 20 frames per flapping period.

2.3. Unsteady forces acting on the flagpole

A particular attention was devoted to the design of a rigid force measurement system (balance) which consists of a flagpole connected to four piezoelectric force sensors Kistler 9712B5 (load cells) which only record force fluctuations (no time-averaged value).

The force sensors are connected to an acquisition system PAK provided by Müller-BBM, whose sampling rate is 1024 acquisitions per second. The duration of acquisition is 14 s: for a flag flapping at 10 Hz, this includes 140 flapping periods. Concerning frequency analysis, noise is reduced by treating independently six blocks of 4 s (with an overlap of 50%); the resulting frequency resolution is then 0.25 Hz.

Linear combinations of the four signals of force sensors are done to reconstruct the unsteady drag force $D(t)$–$\langle D(t)\rangle$ and the unsteady moment (torque) around the flagpole $M(t)$–$\langle M(t)\rangle$, where $\langle\cdots\rangle$ means time-averaged value. Note that $\langle M(t)\rangle$ is generally zero (for symmetric flapping), whereas $\langle D(t)\rangle$ is generally positive. The linear combinations are identified out of wind tunnel, with a calibration based on standard deviations ("root-mean-square" deviations):

$$\sigma_D = \sqrt{\langle D(t)^2\rangle - \langle D(t)\rangle^2}, \quad \sigma_M = \sqrt{\langle M(t)^2\rangle - \langle M(t)\rangle^2}.$$

Known periodic forces and moments are applied to the flagpole by using several spring–mass oscillators. Applied forces are measured with a fifth force sensor (PCB 208C01). The validation of the calibration procedure can be appreciated in Fig. 3, where the applied forces are compared to the reconstructed ones. The frequency range explored during calibration is $f =$ 2–5 Hz and the unsteady force range explored is characterized by $\sigma_D = 40$–140 mN and $\sigma_M = 10$–200 mN m. The worst error

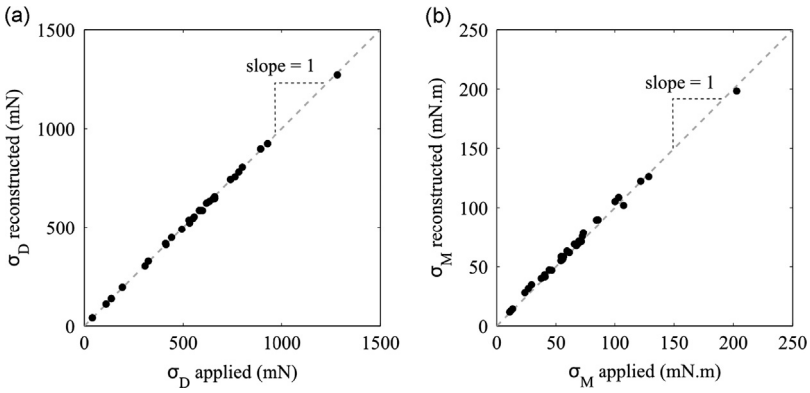

Fig. 3. Calibrations of unsteady forces characterized by their standard deviations: (a) unsteady drag force; (b) unsteady moment around the flagpole; dashed lines are guides for eyes.

is then 7% for σ_D and 9% for σ_M. According to the high sensitivity of the piezoelectric force sensors (deviation from linearity less than 1% in the range 0.5–20 000 mN), the calibration is assumed to be valid in the force range of our experiments: $\sigma_D = 1$–200 mN and $\sigma_M = 1$–5 mN m.

During wind tunnel tests, measurements can be corrupted by resonance between the natural frequencies of the force measurement system and the flag flapping frequency. The first natural frequency of the force measurement system is approximately 90 Hz. Consequently, we select flags having a low-frequency flutter in order to avoid interactions with the force measurement system. Signals from sensors are also filtered to keep an immaculate frequency range 0–60 Hz.

Another corruption might come from vortex-induced forces generated at the flagpole. The flag is somewhat like a splitter plate (see Shukla et al., 2009), and thus vortex shedding only occurs on the lower part of the flagpole. According to the rectangular geometry of the flagpole, vortex shedding is characterized by a constant Strouhal number $\mathrm{St} = fe/U$ close to 0.1 (Hémon, 2006), where e is the flagpole thickness ($e = 4$ mm). Vortex shedding is thus generated with a frequency larger than 200 Hz in the wind velocity range of our experiments. In practice, the motion observed during wind tunnel tests is well dominated by a low frequency flutter ($f \leq 50$ Hz).

2.4. Measurement process

Let us illustrate the measurement process with a concrete example. For this purpose, we select a flag of length $L = 140$ mm fluttering at a wind velocity $U = 8.6$ m/s. The reconstruction of unsteady drag force and moment around the flagpole is shown in Fig. 4(a) and (b). We first notice that unsteady fluid forces are quasi-periodic and that the period for the moment around the flagpole is larger than the period of the drag.

To analyze more deeply unsteady fluid force signals, a frequency analysis based on Power Spectral Densities (P.S.D.) is performed with $\mathrm{P.S.D.} = |\mathrm{F.F.T.}(X)|^2/T$, where $X(t)$ refers to either $D(t)$ or $M(t)$, F.F.T. is the Fast Fourier Transform and T is the duration of $X(t)$. The power spectral densities of unsteady fluid forces are shown in Fig. 4(c) and (d), showing clearly that the dominant frequency of unsteady drag ($\simeq 38$ Hz) is twice the dominant frequency of unsteady moment ($\simeq 19$ Hz). This means that, unsurprisingly, a flapping to the left and a flapping to the right influence the drag identically. Standard deviations of full temporal signals are, respectively, $\sigma_D \simeq 18$ mN and $\sigma_M \simeq 1.2$ mN m. The square root of the integral of power spectral density over the frequency domain gives back the same standard deviations, as predicted by Parseval's identity.

In the present paper, standard deviations and power spectral densities of unsteady fluid forces will be studied as a function of flag length in Section 3 and as a function of wind velocity in Section 4.

3. Unsteady fluid force evolution with flag length

In this section, we start by introducing suitable dimensionless parameters. Then, unsteady fluid forces existing along the boundary of flutter instability are discussed. This boundary is explored by varying the length of the flag.

3.1. Choice of dimensionless parameters

Previous studies emphasized the role of some dimensionless parameters which compare the roles of inertia, elasticity and fluid pressure on the flag. Firstly, the flag length L is usually expressed by a fluid–solid mass ratio (see Eloy et al., 2007; Tang and Païdoussis, 2007; Michelin et al., 2008):

$$M^* = \frac{\rho_a L}{\rho_p d}, \tag{1}$$

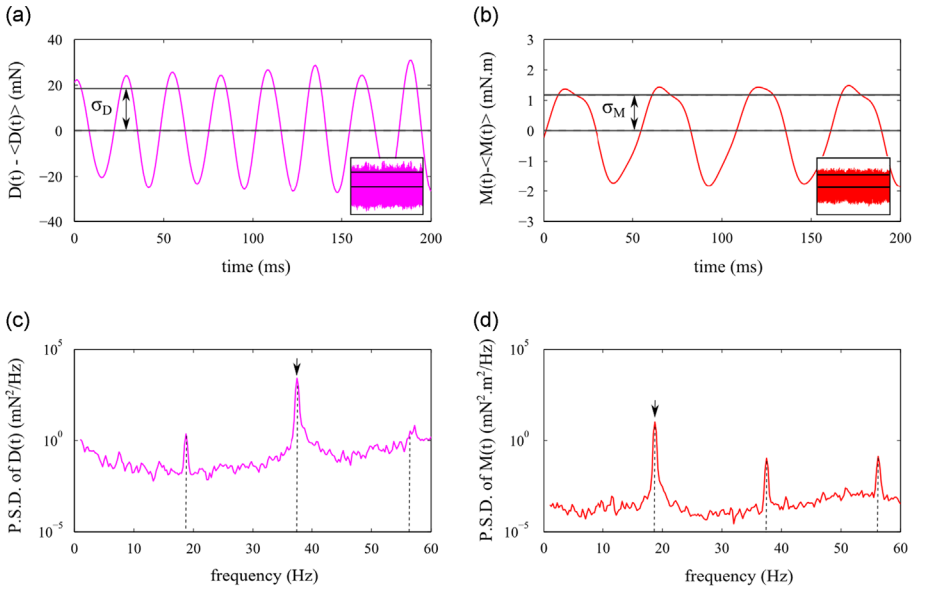

Fig. 4. An example of unsteady force measurement in the case of a flag of length $L = 140$ mm fluttering at a wind velocity $U = 8.6$ m/s: (a) selection of 200 ms from the reconstruction of unsteady drag force; full temporal signal in the inset (14 s); (b) unsteady moment around the flagpole; (c,d) respective power spectral densities of full temporal signals, in logarithmic scale; arrows and vertical dotted lines indicate dominant frequencies.

where d is the flag thickness and ρ_a, ρ_p, respectively, stand for the mass density of air and flag (paper). Accordingly, the mass ratio compares the displaced fluid mass to the displaced solid mass. It arises naturally from a two-dimensional stability analysis (see Eloy et al., 2007).

Then, it is instructive to compare the wind velocity U to the characteristic phase velocity of in vacuo bending waves of the flag $U_\varphi = \sqrt{\mathcal{D}/\rho_p d}/L$, where $\mathcal{D}$ is the flexural rigidity of the flag (Landau and Lifshitz, 1986). The quantity $U^* = U/U_\varphi$ compares characteristic time of free vibration ($\sim \sqrt{\rho_p d/\mathcal{D}L^2}$) – which balances flag inertia and elasticity – to passing time of fluid along the flag ($\sim L/U$) (see Tang and Païdoussis, 2007)

$$U^* = \sqrt{\frac{\rho_p d}{\mathcal{D}}} LU. \tag{2}$$

Another choice of dimensionless parameters is widespread: the mass ratio can be defined by $1/M^*$ and a dimensionless velocity is given by $U^*\sqrt{M^*}$ (see Connell and Yue, 2007; Alben and Shelley, 2008)

$$U^*\sqrt{M^*} = \sqrt{\frac{\rho_a L^3}{\mathcal{D}}} U. \tag{3}$$

This second dimensionless velocity balances characteristic fluid pressure force ($\sim \rho_a U^2 HL$) to characteristic elastic restoring force ($\sim \mathcal{D}H/L^2$), and turns out to be constant in the low M^* limit (see Argentina and Mahadevan, 2005; Alben and Shelley, 2008).

An additional dimensionless number $H^* = H/L$ was introduced in order to assess the relevance of slender flag models ($H^* \ll 1$) as opposed to two-dimensional flag models ($H^* \gg 1$) (see Eloy et al., 2007).

In the present paper, the indication of dimensionless numbers (M^*, U^*), when it is possible, is intended to facilitate the comparison with most of previous and forthcoming studies. We do not work at H^* fixed during our experiments but at M^*H^* fixed (with $M^*H^* = 1.0$), and we vary independently M^* (or H^*) in Section 3 (here) and U^* in Section 4.

3.2. Onset of flutter

The mass ratio is varied in the range $M^* = 0.7$–2.8 by cutting a flag of initial length $L = 290$ mm down to $L = 70$ mm, by increments of 10 mm. The resting state of flags is straight, but a small spanwise twist $\leq 5^\circ$ is visible on the longest flags. The initial flag is not removed from the flagpole between each measurement in order to reduce the influence of flagpole fixation on the flag flexural rigidity.

When increasing wind velocity for a given length, the flag remains straight below a critical flutter velocity of the wind U_{cf}. When decreasing wind velocity, the flag returns to a straight position at a critical rest velocity of the wind U_{cr} always lower than the critical flutter velocity U_{cf}. The scenario observed here (hysteresis) was systematically reported in previous experiments (see Watanabe et al., 2002a).

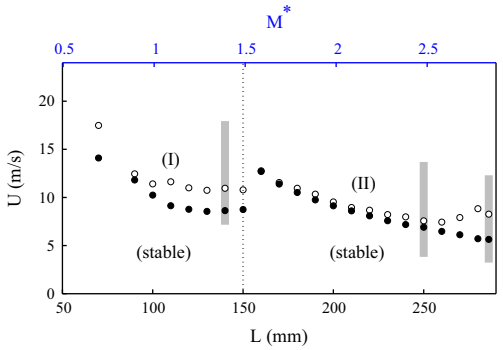

Fig. 5. Critical flutter velocity U_{cf} (○) and critical rest velocity U_{cr} (•) as a function of the flag length L: regimes (I) and (II) are defined in Section 3.4; the three thick bars correspond to the flags studied in Section 4.

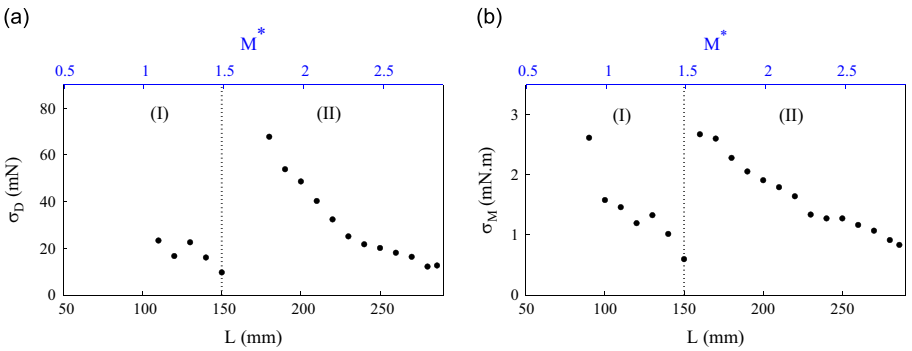

Fig. 6. Evolution of unsteady fluid forces characterized by their standard deviations at the critical rest velocity (defined in Fig. 5): (a) unsteady drag force; (b) unsteady moment around the flagpole; regimes (I) and (II) are defined in Section 3.4.

The presence of a hysteresis loop at the onset of flutter was recently attributed to wake memory effects (see Zhang et al., 2000; Tang and Païdoussis, 2007; Alben and Shelley, 2008; Michelin et al., 2008), structural damping (Alben and Shelley, 2008) and flatness defects (see Tang and Païdoussis, 2007; Eloy et al., 2008, 2012).

The evolution of U_{cf} and U_{cr} in our experiments is shown in Fig. 5, where we observe a discontinuity at $M^* \simeq 1.5$. This discontinuity is well documented for flags (see Yamaguchi et al., 2000a,b; Eloy et al., 2007) and also appears in vertical ribbons (Lemaitre et al., 2005) and in fluid conveying pipes (Doaré and de Langre, 2002). In all these works, a global stability analysis of the flag – i.e. taking into account boundary conditions – in an inviscid flow is sufficient to catch the discontinuity.

3.3. *Unsteady fluid forces at the critical rest velocity (U_{cr})*

Unsteady drag force and moment around the flagpole are measured along the boundary of instability. We focus on forces at critical rest velocity U_{cr} which are apparently less dependent on flatness defects and thus more repeatable than at critical flutter velocity U_{cf}. Results reported in Fig. 6(a) and (b) show that the evolution of unsteady fluid forces with flag length L follows a trend similar to the one of the critical rest velocities U_{cr} (Fig. 5). A huge discontinuity is observed at $M^* \simeq 1.5$ and standard deviations of drag force and moment around the flagpole decrease with flag length before and beyond the discontinuity.

3.4. *Mode switches (type 1)*

Global stability analysis and experiments of Eloy et al. (2008) have recently highlighted that the discontinuity in Fig. 5 is related to a switch of flutter mode. We looked for this flutter mode switch by using a high-speed video camera. Snapshot superimpositions are presented in Fig. 7 for $M^* \simeq 0.69, 1.49, 1.59$ and 2.84 (the corresponding parameters are reported in Table 1). Necks are defined by regions where flapping amplitudes are locally smaller, by analogy with vibration nodes of excited strings. We clearly see a modification of the number of necks in the envelope of flutter mode. One neck of vibration is visible for $0.7 \lesssim M^* \lesssim 1.5$, as in Fig. 7($\alpha$) and ($\beta$); this regime is called regime (I). Two necks are visible when $1.5 \lesssim M^* \lesssim 2.8$, as in Fig. 7($\gamma$) and ($\delta$); this regime is called regime (II). Note that necks are less visible in Fig. 7(δ), where the flag sustains a gentle axial twist due to gravity.

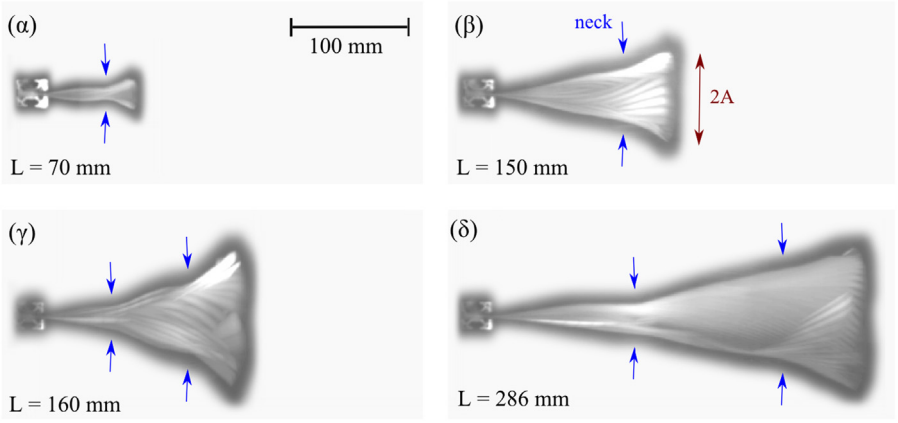

Fig. 7. Snapshot superimpositions (envelopes) in the situation of flags fluttering at the critical rest velocity (defined in Fig. 5), showing the transition from the one-neck regime to the two-neck regime; see also Table 1.

Table 1
Selection of four flags fluttering at the critical rest velocity; Greek letters refer to figure panels (Fig. 7).

Designation	Fig. 7(α)	Fig. 7(β)	Fig. 7(γ)	Fig. 7(δ)
L (mm)/M^*/H^*	70/0.69/1.43	150/1.49/0.67	160/1.59/0.63	286/2.84/0.35
U_{cr} (m/s)/U^*_{cr}	14.1/8.3	8.7/11.0	12.7/17.1	5.6/13.5
f (Hz)	57	17	32	9.5

Envelopes observed in Fig. 7 are similar to the ones observed experimentally by Eloy et al. (2008), and they are also consistent with modifications of envelopes predicted by varying mass ratio (see Huang, 1995; Tang and Païdoussis, 2007; Michelin et al., 2008; Michelin and Llewellyn Smith, 2010; Huang and Zhang, 2013).

3.5. Flapping amplitude

Flapping amplitude (peak-to-peak) of the flag trailing edge is reported in Fig. 8. It is almost constant ($2A \simeq 30$ mm) in regime (I) and also in regime (II) ($2A \simeq 100$ mm). Thus, it does not explain the decrease of unsteady fluid forces in regimes (I) and (II) observed in Fig. 6. On the other hand, we observe that the flutter mode switch is associated with a strong increase of flapping amplitude ($\times 3.3$) which amplifies the discontinuity of unsteady drag and moment around the flagpole at $M^* \simeq 1.5$.

3.6. Frequency analysis

Evolutions of power spectral densities are shown in Fig. 9(c) and (d). In these figures, each vertical slice is a power spectral density similar to the illustrative example given in Fig. 4, Section 2.4. Power spectral densities display sharp peaks (dark color) which indicate a highly periodic flapping. On the other hand, the presence of subharmonics in the power spectral density of unsteady drag indicates that the flapping is not perfectly symmetric in our experiments. At $M^* = 1.5$, the flutter mode switch is associated with a frequency switch visible on power spectral densities: this is consistent with Watanabe's theoretical work (see also Gibbs et al., 2012).

From this section, we can conclude that the discontinuity of unsteady fluid forces which occurs along the boundary of instability at $M^* \simeq 1.5$ corresponds to a transition from the one-neck to the two-neck flutter mode.

4. Unsteady fluid force evolution with wind velocity

The previous section was devoted to the examination of unsteady fluid forces at the boundary of flutter instability. Beyond this boundary, the flag motion is determined by strong structural and fluid non-linearities induced by large deformations. As recently highlighted by Eloy et al. (2012), non-linear dynamics of flags are still obscure. In this context, the present section is devoted to the evolution of unsteady drag force and moment in post-critical conditions and to the corresponding flag dynamics observed.

4.1. Post-critical flutter

Three flags from Section 2 were studied. One flag was selected in the regime (I) of Fig. 5 (one-neck flutter), with a mass ratio $M^* = 1.39$ (Flag 1). This flag has a relatively low critical rest velocity which allows the study of its flutter in a wider

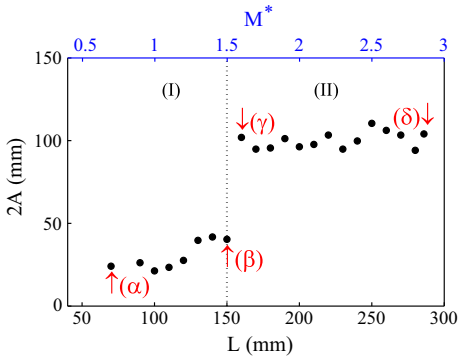

Fig. 8. Flapping amplitude (peak-to-peak) of the flag trailing edge at the critical rest velocity (defined in Fig. 5): Greek letters (α), (β), (γ) and (δ) refer to the snapshots of Fig. 7; see also Table 1.

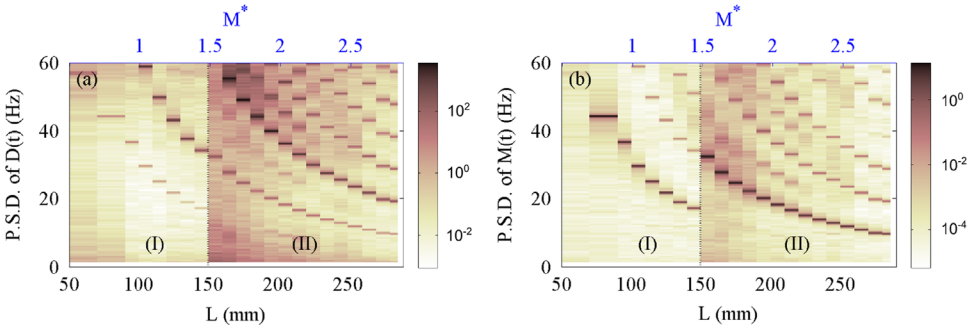

Fig. 9. Evolution of power spectral densities at the critical rest velocity (defined in Fig. 5): (a) unsteady drag force; (b) unsteady moment; the color scale is logarithmic in mN^2/Hz and $mN^2\ m^2/Hz$, respectively. (For interpretation of the references to color in this figure caption, the reader is referred to the web version of this article.)

Table 2
Selection of three flags for wind velocity dependence tests.

Designation	Flag 1	Flag 2	Flag 3
L (mm)/M^*/H^*	140/1.39/0.71	250/2.48/0.40	286/2.84/0.35
U (m/s)/U^*	7.2–17.9/8.5–21.1	3.8–13.7/8.0–28.9	3.2–12.3/7.6–29.6
U_{cf1} (m/s)/U^*_{cf1}	10.1/11.9	–	–
U_{cf2} (m/s)/U^*_{cf2}	15.0/17.7	9.0/18.9	6.4/15.4
U_{cf3} (m/s)/U^*_{cf3}	16.7/19.7	11.4/24.0	10.1/24.3
U_{cf4} (m/s)/U^*_{cf4}	–	12.6/26.5	10.9/26.2

range of wind velocities in the wind tunnel. Two other flags were selected in the regime (II) of Fig. 5 (two-neck flutter) with $M^* = 2.48$ (Flag 2) and $M^* = 2.84$ (Flag 3). Both have relatively low critical rest velocity and Flag 3 corresponds to the longest flag that can be studied in the wind tunnel. Parameters associated with these flags are reported in Table 2. For each flag, wind tunnel tests were done for a wind velocity increasing up to the velocity for which the flag tears, as done by Watanabe et al. (2002a). Standard deviations of unsteady drag force (σ_D) and unsteady moment around the flagpole (σ_M) are presented in Fig. 10.

The first set of experiments was conducted with Flag 1 (Fig. 10(a) and (b)). At $U = 10.1$ m/s, this is the onset of flutter and we observe a discontinuity of σ_D and σ_M followed by a gentle increase. There is a strong and sharp increase of σ_M at $U = 15.0$ m/s. A sharp increase in σ_D was also observed at $U = 15.0$ m/s, but due to the proximity between the flapping frequency and the cut-off frequency of our measurement system (60 Hz) these flawed data are removed. Another experiment was performed with the same flag (empty circles in Fig. 10). On the one hand, we can notice that the critical velocity is significantly higher for the second test. This discrepancy is attributed to flatness defects almost impossible to avoid in practice (Eloy et al., 2012). On the other hand, comparable levels of forces are found when the flag flutters.

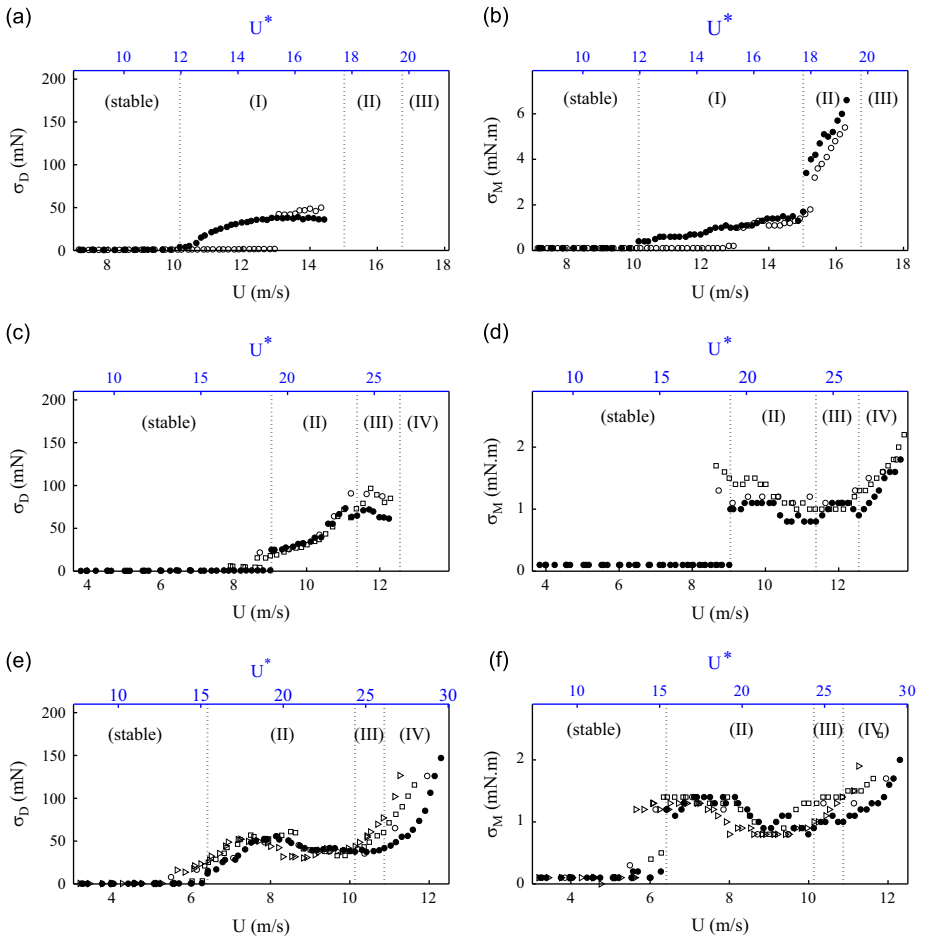

Fig. 10. Evolution of unsteady drag force and moment around the flagpole, characterized by their standard deviations, when the wind velocity is increased: (a, b) Flag 1; (c, d) Flag 2; (e, f) Flag 3; empty symbols correspond to repeatability tests; regimes (I), (II), (III) and (IV) are defined in Section 4.2; see also Table 2.

The second set of experiments was conducted on Flag 2 (Fig. 10(c) and (d)). Beyond the critical flutter velocity $U = 9.0$ m/s, we observe that σ_D increases with the wind velocity for $U \leq 11.4$ m/s, and then slightly decreases. Above $U = 12$ m/s, data are flawed and removed (cut-off frequency). In the same time and after a strong discontinuity at $U = 9.0$ m/s, σ_M decreases slowly for $U \leq 11.4$ m/s, remains almost constant for $11.4 \leq U \leq 12.6$ m/s and then increases for $U \geq 12.6$ m/s. Two other experiments were performed with the same flag (empty circles and squares in Fig. 10), and comparable evolutions and levels of forces are obtained.

The third set of experiments was conducted on Flag 3 (Fig. 10(e) and (f)). Beyond the critical flutter velocity $U = 6.4$ m/s, we observe a discontinuity followed by a gentle increase of σ_D for $U \leq 8$ m/s. Then, σ_D slowly decreases for $U \leq 10.1$ m/s, and then strongly increases. In parallel and after a strong jump at $U = 6.4$ m/s, σ_M is slowly decreasing for $U \leq 10.1$ m/s, and then it increases. Three other experiments were performed with the same flag (empty circles, squares and triangles in Fig. 10), and comparable evolutions and levels of forces are obtained as well.

Unsurprisingly, unsteady fluid forces are very low when the flag is not fluttering (regimes called (stable) in Fig. 10): $\sigma_D \leq 1$ mN and $\sigma_D \leq 0.1$ mN m.

The next parts of the present section will discuss the evolution of unsteady fluid forces (Fig. 10) by reporting the presence of mode switches and by analyzing flapping amplitudes and power spectral densities (flapping frequencies).

4.2. Mode switches (type 2)

Flutter mode switches due to an increase of wind velocity (at a given mass ratio M^*) were photographed and examined for the first time by Taneda (1968) on vertical flags, they were highlighted in recent experiments (see Eloy et al., 2008; Gomes and Lienhart, 2013), and they were predicted numerically as well (see Fitt and Pope, 2001; Yadykin et al., 2001; Connell and Yue, 2007; Alben and Shelley, 2008; Michelin et al., 2008). In practice, the fast motion of flags blurs visual observation and prevents a simple visual detection of flutter mode switches. However, by using a high-speed video camera

Table 3
Wind velocities applied to Flag1; Greek letters refer to figure panels (Fig. 11).

Designation	Fig. 11(α)	Fig. 11(β)	Fig. 11(γ)	Fig. 11(δ)	Fig. 11(ε)	Fig. 11(ζ)
U (m/s)/U^*	9.2/10.9	11.5/13.6	14.9/17.6	15.0/17.7	16.9/20.0	17.3/20.4
f (Hz)	0	23	30	32	58	57

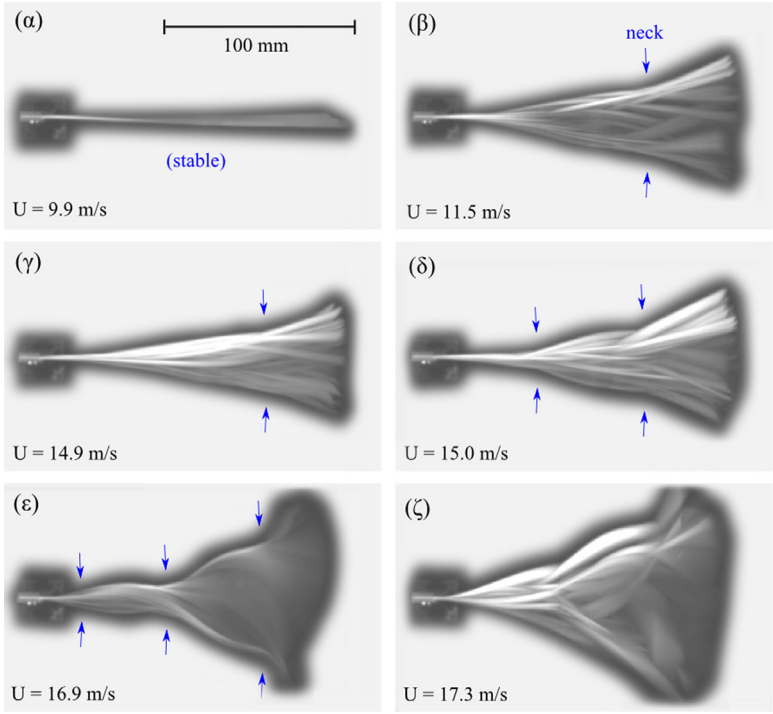

Fig. 11. Snapshot superimpositions (envelopes) of Flag 1 showing the onset of one- two- and three-neck flutter mode, followed by a loss of periodicity; see Table 3.

in the situation of Flag 1, Flag 2 and Flag 3, flutter modes can be easily detected because they are characterized by a constant number of necks. This is not surprising that each flutter mode has a given number of necks: by using the Galerkin method we can show that flutter modes correspond to specific projections on in vacuo cantilever beam modes (see Howell et al., 2009; Huang and Zhang, 2013).

We can thus define regimes (I), (II), (III) and (IV), the one-, two-, three-, and four-neck flutter regime along with U_{cf1}, U_{cf2}, U_{cf3} and U_{cf4}, the wind velocity for the onset of each regime (see Table 2). In snapshot superimpositions of Fig. 11 the successive flutter mode switches for Flag 1 can be appreciated. When the wind velocity increases, one-neck flutter (Fig. 11(β) and (γ)) is succeeded by two-neck flutter (Fig. 11(δ)) and three-neck flutter (Fig. 11(ε)). The last regime before tear (Fig. 11(ζ)) is characterized by a succession of quasi-periodic and "chaotic" oscillations, and the flag undergoes snapping events: this will be discussed in Section 4.6.

For both Flag 2 and Flag 3, high-speed video analysis suggests that the two-neck flutter regime – which comes beyond the critical flutter velocity – is succeeded by three-neck flutter and four-neck flutter (not shown).

4.3. *Flapping amplitude*

The evolution of flapping amplitude for Flag 1 is reported in Fig. 12. When increasing the wind velocity above the onset of flutter, the flapping amplitude first increases and reaches almost a constant value $2A \simeq 60$ mm for $12 \lesssim U \lesssim 14$ m/s. When $U \gtrsim 14$ m/s, the reduction of flapping amplitude reflects the change of envelope before the onset of two-neck flutter, as observed when Fig. 11(β) is compared to Fig. 11(γ). After the onset of the two-neck regime (Fig. 11(δ)), the flapping amplitude suddenly reaches $2A \simeq 80$ mm and increases again for higher wind velocity.

Flapping amplitudes of Flag 2 and Flag 3 are reported in Fig. 13(a) and (b), respectively. For both flags the onset of flutter (two-neck regime) is characterized by high flapping amplitudes $2A \geq 150$ mm. When increasing the wind velocity, the flapping amplitude remains constant for Flag 2 until the switch to the three-neck flutter regime where it slightly decreases.

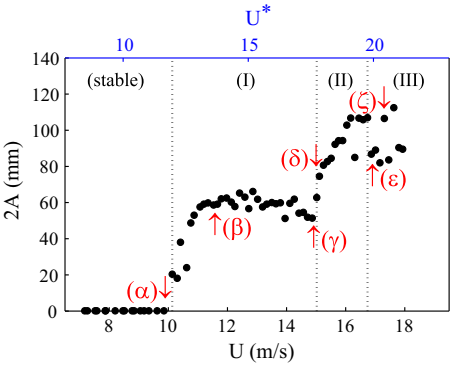

Fig. 12. Flapping amplitude (peak-to-peak) of the flag trailing edge when the wind velocity is increased in the situation Flag 1: arrows (α), (β), (γ), (δ), (ε) and (ζ) refer to snapshots of Fig. 11; see also Table 3.

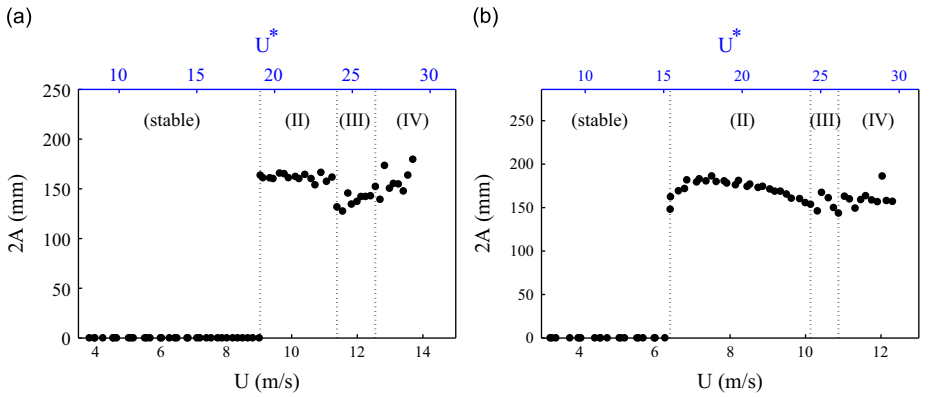

Fig. 13. Flapping amplitude (peak-to-peak) of the flag trailing edge when the wind velocity is increased: (a) Flag 2; (b) Flag 3.

Then, it increases again in the four-neck regime. For Flag 3, we can notice a small bump of flapping amplitude at $U \simeq 7.5$ m/s which is associated with the change of envelope before the onset of the three-neck regime.

Note that flapping amplitudes of Flag 2 and Flag 3 are closed to the wind tunnel width (240 mm), and thus a deterioration of vortical dynamics is possible (see Tang and Païdoussis, 2007). Data for Flag 2 and Flag 3 have thus to be taken with caution.

4.4. Frequency analysis

To better understand the evolution of unsteady fluid forces (Fig. 10), we analyze the evolution of their power spectral densities when increasing the wind velocity. Results for Flag 1 are reported in Fig. 14(a) (unsteady drag) and in Fig. 14(b) (unsteady moment around the flagpole). In Fig. 14(a) we observe a dominant frequency which grows almost linearly from 40 Hz, and a subharmonic frequency which suggests that the flapping is not perfectly symmetric. In Fig. 14(b), the dominant frequency grows from 20 Hz, and is shifted upward at $U = 15.0$ m/s (transition from the one-neck to the two-neck regime) and also at $U = 16.7$ m/s (transition from the two-neck to the three-neck regime). Unsurprisingly, the dominant frequency of the moment around the flagpole (in Fig. 14(b)) was always equal to the flapping frequency observed with a high-speed video camera. Once two-neck flutter is established at $U = 15.0$ m/s, we observe a loss of periodicity in Fig. 14(b), where the power spectral density spreads.

In the situation of Flag 2 and Flag 3, in Fig. 14(c–f), dominant frequencies are not strongly shifted, but the period of "hesitation" between two-neck flutter and three-neck flutter is striking on power spectral densities, where we observe a "gap" of dominant frequency, respectively, at $U = 11.4$ m/s and at $U = 10.1$ m/s. Despite appearance, the flag is still flapping during this "gap". From Fig. 14(e), we note that the small decrease of σ_D at $U \simeq 8$ m/s in Fig. 10(e) is partly due to the cut-off frequency 60 Hz applied on the fourth harmonics (artefact).

The motion of the flags is less and less periodic after the first mode switch, where power spectral densities start to spread. This illustrates the non-linear nature of flag dynamics at high wind velocities. The underlying mechanism of flutter mode switches is presumably different from one of the switches induced by mass ratio variations in Section 3 (essentially linear).

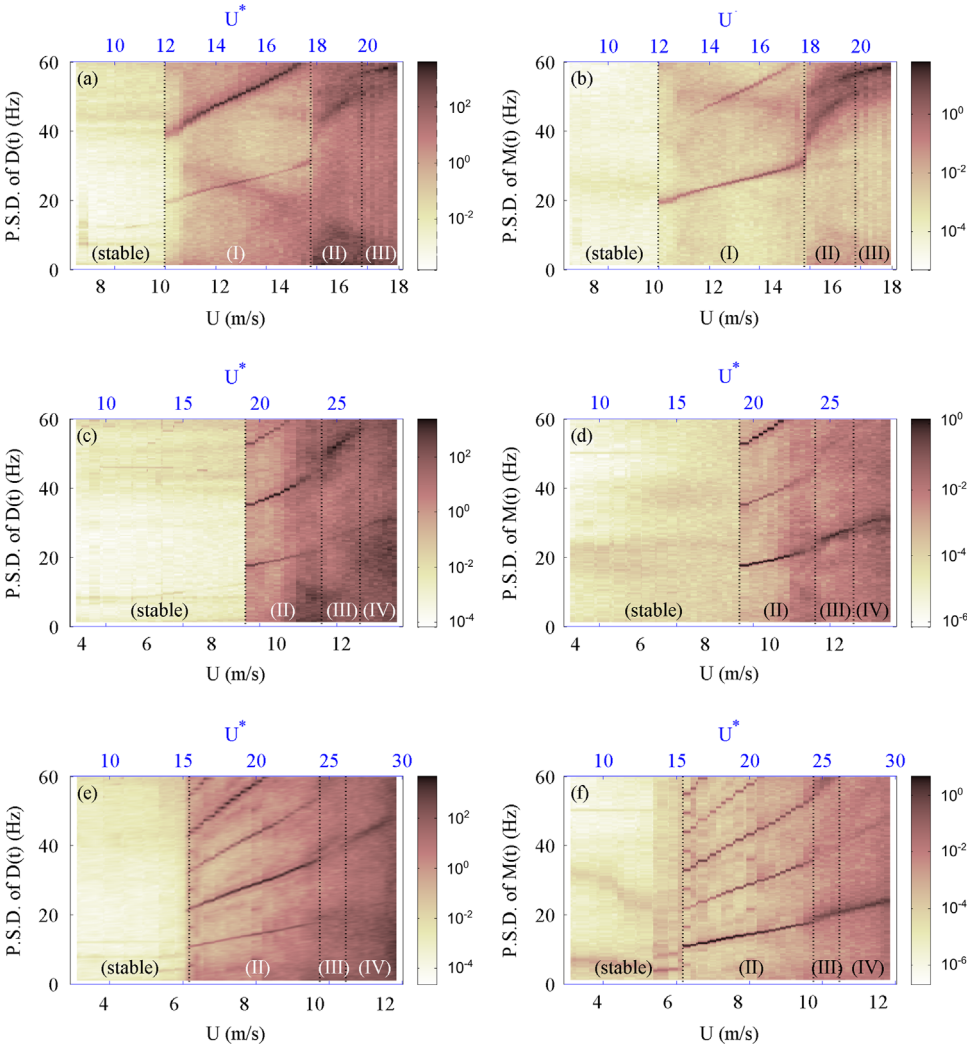

Fig. 14. Evolution of power spectral densities of unsteady drag force and moment around the flagpole, when the wind velocity is increased: (a, b) Flag 1; (c, d) Flag 2; (e, f) Flag 3; the color scale is logarithmic in mN^2/Hz and $mN^2\,m^2/Hz$, respectively; see also Table 2. (For interpretation of the references to color in this figure caption, the reader is referred to the web version of this article.)

In the example proposed in Fig. 4, Section 2.4, we have discussed the fact that the dominant frequency of unsteady drag force is twice the dominant frequency of unsteady moment around the flagpole. More precisely, we observe here that the power spectral density of unsteady moment around the flagpole has always dominant odd frequencies $(1\times f, 3\times f, 5\times f, \ldots)$ whereas the power spectral density of the unsteady drag force has always dominant even harmonics $(2\times f, 4\times f, \ldots)$. This is consistent with the symmetry of flapping, as in the theoretical study of Michelin et al. (2008), where the flag tail orientation spectrum has dominant odd harmonics whereas the total energy spectrum contains dominant even harmonics.

Some other features are observed on power spectral densities, but would require further investigation, such as the apparent coalescent frequencies in the range $U\simeq 10$–15 m/s in Fig. 14(b), or before the onset of flutter in the range $U\simeq 4$–6 m/s in Fig. 14(f).

4.5. Note on the reduced frequency

It is instructive to compare the time-scale ratio of the fluid passing along the flag ($=L/U$) to the flapping period ($=1/f$). This defines the reduced frequency $f^*=fL/U$.

The evolution of reduced frequency with wind velocity is presented in Fig. 15. The range of reduced frequencies measured $f^*=0.2$–0.6 is fairly close to 1, suggesting a strong coupling between the flag and the fluid (a significant time-delay of the fluid response is likely).

We observe that f^* is almost constant in each flutter mode. Indeed, dominant frequencies increase linearly with the wind velocity in each flutter regime, as shown in Fig. 14. This linearity between flapping frequency and wind velocity was

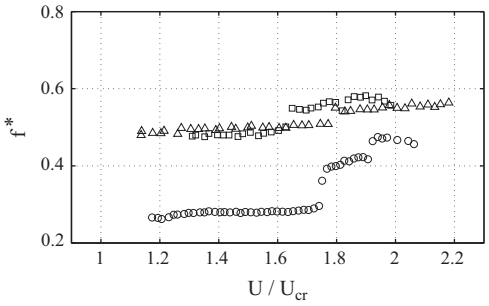

Fig. 15. Evolution of the reduced frequency when the wind velocity is increased (data from Fig. 14): Flag 1 (○), Flag 2 (□), Flag 3 (▵); see also Table 2.

evidenced long ago in experiments performed by Taneda (1968) and Uno (1973). Recently, this was confirmed for flags fluttering in flowing water, for a mass ratio $M^* \simeq 3 \times 10^4$ (Shelley et al., 2005). This linearity is also well predicted by an elementary local analysis at fixed mass ratio (see Coene, 1992; Triantafyllou, 1992; Connell and Yue, 2007): the reduced frequency f^* is a constant of wind velocity, and the value of the constant depends only on the flutter mode (see also the non-linear analyzes done by Tang et al., 2003; Tang and Païdoussis, 2007; Michelin and Doaré, 2013). Accordingly, we observe a reduced frequency staircase-shaped in Fig. 15.

4.6. Note on the loss of periodicity and snapping events

By comparing Fig. 14 to Fig. 10, we observe that unsteady fluid forces are stronger when the flapping is no more periodic, that is to say approximately after the first flutter mode switch. The loss of periodicity was initially observed by Taneda (1968) who noted that "[…] the oscillation becomes violent and irregular. […]". This is also widely predicted (see Yadykin et al., 2001; Connell and Yue, 2007; Alben and Shelley, 2008; Michelin et al., 2008; Huang and Sung, 2010), and recently Eloy et al. (2012) suggested that the loss of periodicity arises from a non-linear interaction between two modes of comparable frequency. Both experimental and numerical studies report systematically three regimes when increasing the wind velocity: stability, periodic flapping, and finally chaotic flapping (see the recent experiments of Zhao et al., 2012; Ait Abderrahmane et al., 2012). This is actually common that flexible structures which undergo a large excitation exacerbates chaotic properties, as observed in the context of musical instruments (Touzé et al., 2012). However, regimes observed at the highest wind velocities of our experiments still have a dominant frequency (see Fig. 14): the periodicity is just strongly reduced by spread of frequencies around the dominant frequency.

When the periodicity is lost, we have detected the presence of several snapping events, that is to say fast and large accelerations of the flag trailing edge. For the Flag 3 and according to the power spectral densities of Fig. 14(e) and (f), a loss of periodicity is expected for $U \gtrsim 10.1$ m/s. To illustrate this situation, unsteady fluid force signals and their associated power spectral densities are presented in Fig. 16 for $U = 12.3$ m/s. The unsteady drag force signal is characterized by $\sigma_D = 180$ mN, meaning that maxima would be $\sqrt{2} \times \sigma_D = 250$ mN in the ideal harmonic case. Instead, in some short intervals of the order of 10 ms, unsteady drag force reaches more than 3 times the ideal value (≥ 800 mN). In parallel, the unsteady moment around the flagpole is smaller than $\sigma_M = 2.7$ mN m during the flapping event, as shown in Fig. 16(b). This suggests that snapping events are essentially longitudinal accelerations. These violent accelerations are probably at the origin of the flag tear.

5. Drag coefficients of flags

In this last section, we report measurements of time-averaged drag coefficients. They are discussed in the light of the analysis of unsteady fluid forces. A comparison with previously reported drag coefficients is done.

5.1. Time-averaged drag coefficient

Time-averaged drag forces were measured in the same wind tunnel by using a force measurement system based on strain gauges. Results are presented in the usual form of aerodynamic coefficients:

$$\langle C_D \rangle = \frac{\langle D(t) \rangle}{\frac{1}{2}\rho_a U^2 S}, \tag{4}$$

where the surface S is chosen to be the flag width $\times$ the flag length ($S = HL$). This convention was used by Fairthorne (1930) and by most works on drag of flags after his contribution.

The evolution of $\langle C_D \rangle$ at the onset of flutter when the flag length is varied is shown in Fig. 17(a). As for the unsteady drag force in Fig. 6(a), Section 3.2, we still observe an increase of $\langle C_D \rangle$ when $M^* = 1.5$ is crossed. This is associated with the flutter

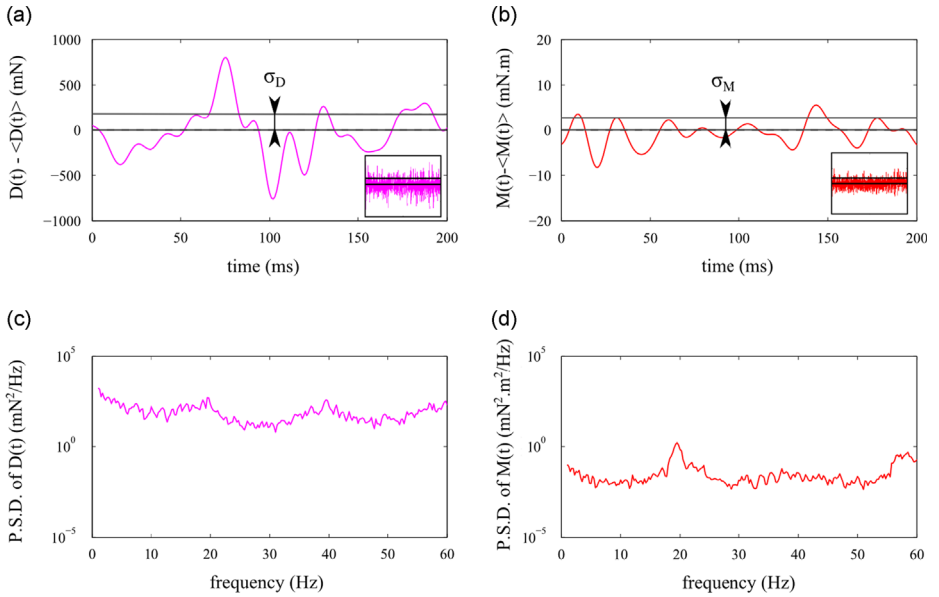

Fig. 16. Snapping events for Flag 3 fluttering at a wind velocity $U = 12.3$ m/s: (a) selection of 200 ms from unsteady drag force; full temporal signal in the inset (14 s); (b) unsteady moment around the flagpole; (c, d) respective power spectral densities of full temporal signals, in logarithmic scale.

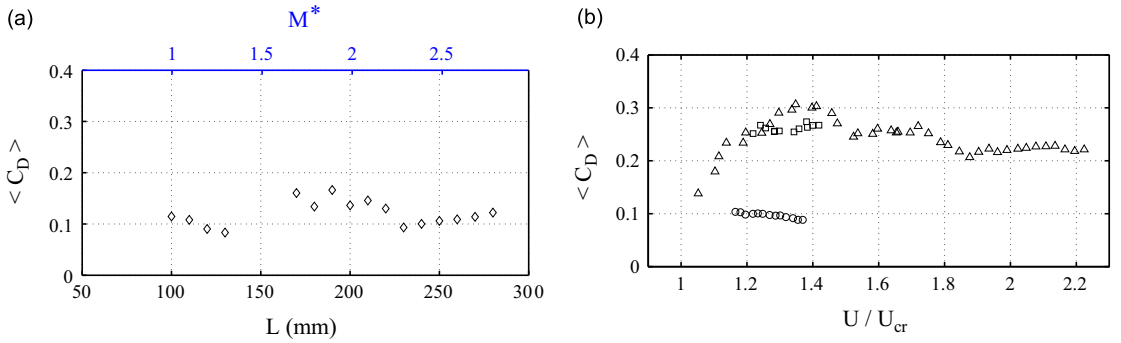

Fig. 17. Evolution of time-averaged drag coefficient: (a) as a function of flag length at the critical rest velocity U_{cr}; (b) when the wind velocity is increased; Flag 1 (○), Flag 2 (□), Flag 3 (▵).

mode switch. For each flutter mode, a gentle decrease is visible, as in experiments of Carruthers and Filippone (2005) and Wilk and Skuta (2009).

When increasing the wind velocity, we measured the evolution of $\langle C_D \rangle$ for Flag 1, Flag 2 and Flag 3. This is reported in Fig. 17(b).

In the situation of Flag 3 (empty triangles in Fig. 17(b)), we observe that $\langle C_D \rangle$ first increases from $\langle C_D \rangle \simeq 0.15$ at $U \simeq 1.05 \times U_{cr}$ up to $\langle C_D \rangle \simeq 0.3$ at $U \simeq 1.4 \times U_{cr}$. Then, it decreases slowly and asymptotically tends toward $\langle C_D \rangle \simeq 0.22$. So the evolution of $\langle C_D \rangle$ of Flag 3 has a small bump close to the onset of flutter, which was also reported by Morris-Thomas and Steen (2009). The bump of $\langle C_D \rangle$ corresponds approximately to the bump of flapping amplitude of Flag 3 in Fig. 13(b), Section 4.3. In the situation of Flag 1 and Flag 2, results are presented in a short wind velocity range $1.1–1.4 \times U_{cr}$. Beyond, data are flawed because of a strong coupling with the measurement system when the flapping frequency crosses 25 Hz. When Flag 2 and Flag 3 are fluttering in the two-neck regime, $\langle C_D \rangle$ is almost 3 times larger than for Flag 1 fluttering in the one-neck regime, in the same range of wind velocities.

5.2. *Unsteady drag coefficient*

We can define similarly the unsteady drag coefficient $\sigma(C_D)$ by

$$\sigma(C_D) = \frac{\sigma_D}{\frac{1}{2}\rho_a U^2 S} \quad \text{with } S = HL. \tag{5}$$

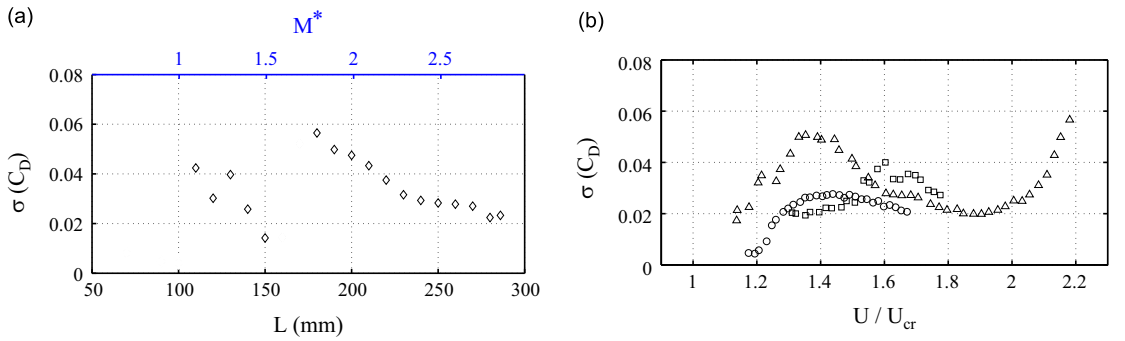

Fig. 18. Evolution of unsteady drag coefficient: (a) as a function of flag length at the critical rest velocity U_{cr} (data from Section 3); (b) when the wind velocity is increased (data from Section 4); Flag 1 (○), Flag 2 (□), Flag 3 (△).

Table 4
Comparison of time-averaged and unsteady drag coefficients at $U \simeq 1.4 \times U_{cr}$.

Flag	Present work		Fairthorne (1930)	Moretti (2003)		Connell (2006)	
	$\langle C_D \rangle$	$\sigma(C_D)$	$\langle C_D^{\text{Fai.}} \rangle$	$\langle C_D^{\text{Mor.}} \rangle$	$\sigma(C_D^{\text{Mor.}})$	$\langle C_D^{\text{Con.}} \rangle$	$\sigma(C_D^{\text{Con.}})$
1	0.09	0.027	0.52	0.05	0.004	0.47	0.36
2	0.27	0.021	0.25	0.22	0.031	0.29	0.18
3	0.30	0.049	0.21	0.14	0.020	0.25	0.14

The evolution of $\sigma(C_D)$ with the flag length is shown in Fig. 18(a) with data from Section 3. We still notice a strong discontinuity due to the flutter mode switch at $M^* \simeq 1.5$ and a decreasing trend in each flutter regime. We can appreciate the evolutions of $\sigma(C_D)$ for Flag 1, Flag 2 and Flag 3 when increasing wind velocity in Fig. 18(b) (data from Section 4). The values of $\sigma(C_D)$ have also a bump whose maximum is located at approximately $1.4 \times U_{cr}$ for Flag 1 and Flag 2, and at $1.6 \times U_{cr}$ for Flag 3. This fairly corresponds to the maxima of flapping amplitudes reported in Section 4.3. In the situation of Flag 3, we note that $\sigma(C_D)$ increases strongly above $1.8 \times U_{cr}$, that is to say the point where we have detected a loss of periodicity in Section 4.4.

It is instructive to compare $\sigma(C_D)$ to $\langle C_D \rangle$ in the situation of Flag 3, in order to get a relative measure of the drag unsteadiness. The ratio $\sigma(C_D) / \langle C_D \rangle$ is typically 10% below $1.8 \times U_{cr}$, with a maximum 15% at the top of the bump at $1.4 \times U_{cr}$. Instead, it reaches 26% in the regime where a loss of periodicity was reported, i.e. above $1.8 \times U_{cr}$.

5.3. Discussion

Some quantitative estimations for time-averaged drag coefficients $\langle C_D \rangle$ are present among previous studies. Fairthorne (1930) provided an empirical formula, based on its own experiments on 13 flags, for mass ratio in the range $M^* \simeq 4.3$–97 and at a constant wind velocity $U = 30.5$ m/s. The skin friction drag contribution being negligible in our case, the Fairthorne formula $\langle C_D^{\text{Fai.}} \rangle$ can be simplified as follows:

$$\langle C_D^{\text{Fai.}} \rangle \simeq 0.78 \frac{(H^*)^{0.25}}{M^*}. \tag{6}$$

This expression does not take into account the wind velocity, but strongly depends on mass ratio. Values of $\langle C_D^{\text{Fai.}} \rangle$ corresponding to Flag 1, Flag 2 and Flag 3 are reported in Table 4, where they are compared with our measurements at $U \simeq 1.4 \times U_{cr}$. In the situation of Flag 3, it gives $\langle C_D^{\text{Fai.}} \rangle = 0.21$ which is significantly lower than the value $\langle C_D \rangle \simeq 0.30$ reported at $U \simeq 1.4 \times U_{cr}$, but it is in very good agreement with the asymptotic value $\langle C_D \rangle \simeq 0.22$ reported in Fig. 17(b). In the situation of Flag 1, we measured $\langle C_D \rangle \simeq 0.09$, much lower than $\langle C_D^{\text{Fai.}} \rangle \simeq 0.52$, but an increase of $\langle C_D \rangle$ is expected with the flutter mode switch from the one-neck regime to the two-neck regime, as observed with unsteady drag force measurements. Finally, our data suggest that the Fairthorne formula is not applicable at the onset of flutter, but that formula is reasonable for high wind velocities, typically above $1.8 \times U_{cr}$ for Flag 3. This is consistent with the fact that the Fairthorne formula was established for large mass ratios $M^* \geq 4.3$ and with a relatively high wind velocity ($= 30.5$ m/s).

More recently, Moretti (2003) adapted the work of Thoma (1939a,b) to suggest an estimation of flag tension from the loss of kinetic energy at the trailing edge. This model neglects the flexural rigidity of the flag. In our case for which $\lambda/L < 2$, where λ is the characteristic wavelength along the flag (classically $\lambda/L \simeq 0.75$ for a one-neck flutter), the model can be simplified:

$$\langle C_D^{\text{Mor.}} \rangle = \frac{2\pi^2}{M^*} \left(\frac{fA}{U} \right)^2, \quad \sigma(C_D^{\text{Mor.}}) \simeq \frac{\pi}{\sqrt{2} M^*} \left(\frac{fA}{U} \right)^2 \frac{\lambda}{L}, \tag{7}$$

where the ratio between the typical transverse velocity of the flag trailing edge ($=fA$) and the oncoming wind velocity ($=U$) depends strongly on the flutter mode. This elementary model was recently validated by experiments with a mass ratio $M^*=0.53$ (Martin, 2006). When compared to our measurements (Table 4), we notice that it predicts the good order of magnitude except for Flag 1.

From recent numerical simulations at $\mathrm{Re}<5\times10^3$, Connell (2006) obtained a fit for both time-averaged and unsteady drag coefficients for mass ratios $M^*\geq1$. In our case, this can be approximated as follows:

$$\langle C_D^{\mathrm{Con.}}\rangle \simeq \frac{0.8}{M^*}\left(1-\left(\frac{2\pi}{U^*}\right)^2\right), \quad \sigma(C_D^{\mathrm{Con.}}) \simeq \frac{1.5}{(M^*)^{1.5}}\left(1-\left(\frac{2\pi}{U^*}\right)^2\right)^{1.5}, \tag{8}$$

where terms depending on the wind velocity can be neglected for sufficiently high wind velocities. The analytic expression $\langle C_D^{\mathrm{Con.}}\rangle$ is very close to the analytic expression $\langle C_D^{\mathrm{Fai.}}\rangle$, and thus gives similar results. Nevertheless, the estimation of $\sigma(C_D^{\mathrm{Con.}})$ is one order of magnitude higher than $\sigma(C_D)$ that we have measured. Moreover, the scaling relationship observed in Fig. 18(a) is $\sigma(C_D)\sim(M^*)^{-2.0}$ in each flutter regime, substantially different from $\sigma(C_D^{\mathrm{Mor.}})\sim(M^*)^{-1}$ or $\sigma(C_D^{\mathrm{Con.}})\sim(M^*)^{-1.5}$.

This quick comparison suggests that further experimental, theoretical and numerical investigations on unsteady forces acting on a flagpole would be beneficial for drawing a complete picture of flag dynamics.

6. Summary

In this paper, unsteady fluid force measurements on flags fluttering in a wind tunnel have been discussed. At the onset of flutter, we have observed that both unsteady drag force and unsteady moment around the flagpole decrease when the flag length is increased, with a strong discontinuity for a mass ratio $M^*\simeq1.5$. We have shown that this discontinuity is associated with a flutter mode switch from the one-neck regime to the two-neck regime. We have also shown that the flutter mode switch induces a doubling of time-averaged drag coefficient and a tripling of unsteady drag coefficient.

When the wind velocity is increased above the critical flutter velocity, we have observed various evolutions of unsteady fluid forces according to the flags considered, but all of them are characterized by a reduced frequency staircase-shaped, i.e. constant for each flutter mode. A bump of time-averaged and unsteady drag coefficients has been detected and has been correlated to a modification of the envelope of flutter mode. For sufficiently high wind velocities, we have shown that the loss of periodicity is correlated with a strong increase of unsteady fluid forces, leading ultimately to a tear of the flag.

Acknowledgments

We are grateful to Clairefontaine company for providing many Clairalfa paper samples and for discussion about their fabrication process. We are grateful to Eric Perrin and Guillaume Puel who helped us to realize the tensile tests of flags and we warmly thank Emmanuel de Langre, Sébastien Michelin, Olivier Doaré and Yifan Xia for helpful discussions on flag models. E.V. acknowledges his financial support from EDX-DGA program.

References

Ait Abderrahmane, H., Païdoussis, M.P., Fayed, M., Ng, H.D., 2012. Nonlinear dynamics of silk and Mylar flags flapping in axial flow. Journal of Wind Engineering and Industrial Aerodynamics 107–108, 225–236.
Alava, M., Niskanen, K., 2006. The physics of paper. Reports on Progress in Physics 69, 669–723.
Alben, S., Shelley, M.J., 2008. Flapping states of a flag in an inviscid fluid: bistability and the transition to chaos. Physical Review Letters 100, 074301.
Alben, S., 2009. Wake-mediated synchronization and drafting in coupled flags. Journal of Fluid Mechanics 641, 489–496.
Argentina, M., Mahadevan, L., 2005. Fluid-flow-induced flutter of a flag. Proceedings of the National Academy of Sciences 102 (6), 1829–1834.
Auman, L., Wilks, B., 2005. Application of fabric ribbons for drag and stabilization. In: 18th AIAA Aerodynamic Decelerator Systems Technology Conference and Seminar, vol. 1618, pp. 1–9.
Bourrières, F.J., 1969. L'onde (du 4ème ordre) de fanion, onde du poisson et du vol en régime. Publications Scientifiques et Techniques du Ministère de l'Air 482, 120–121.
Carruthers, A.C., Filippone, A., 2005. Aerodynamic drag of streamers and flags. Journal of Aircraft 42 (4), 976–982.
Coene, R., 1992. Flutter of slender bodies under axial stress. Applied Scientific Research 49, 175–187.
Connell, B.S.H., 2006. Numerical Investigation of the Flow-Body Interaction of Thin Flexible Foils and Ambient Flow. Ph.D. Thesis, Massachusetts Institute of Technology.
Connell, B.S.H., Yue, D.K.P., 2007. Flapping dynamics of a flag in a uniform stream. Journal of Fluid Mechanics 581, 33–67.
Doaré, O., de Langre, E., 2002. Local and global instability of fluid-conveying pipes on elastic foundations. Journal of Fluids and Structures 16 (1), 1–14.
Doaré, O., Michelin, S., 2011. Piezoelectric coupling in energy-harvesting fluttering flexible plates: linear stability analysis and conversion efficiency. Journal of Fluids and Structures 27, 1357–1375.
Dunnmon, J.A., Stanton, S.C., Mann, B.P., Dowell, E.H., 2011. Power extraction from aeroelastic limit cycle oscillations. Journal of Fluids and Structures 27, 1182–1198.
Eloy, C., Souilliez, C., Schouveiler, L., 2007. Flutter of a rectangular plate. Journal of Fluids and Structures 23, 904–919.
Eloy, C., Lagrange, R., Souilliez, C., Schouveiler, L., 2008. Aeroelastic instability of cantilevered flexible plates in uniform flow. Journal of Fluid Mechanics 611, 97–106.
Eloy, C., Kofman, N., Schouveiler, L., 2012. The origin of hysteresis in the flag instability. Journal of Fluid Mechanics 691, 583–593.
Fairthorne, R.A., 1930. Drag of Flags. Aeronautical Research Committee, Reports and Memoranda vol. 1345, pp. 887–891.
Fancett, R.K., Clayden, W.A., 1972. Subsonic wind tunnel tests on the use of streamers to stabilize the foil bomblet. Royal Armament Research and Development Establishment, Memorandum 14/70.
Fitt, A.D., Pope, M.P., 2001. The unsteady motion of two-dimensional flags with bending stiffness. Journal of Engineering Mechanics 40, 227–248.

Gibbs, S.C., Wang, I., Dowell, E., 2012. Theory and experiment for flutter of a rectangular plate with a fixed leading edge in three-dimensional axial flow. Journal of Fluids and Structures 34, 68–83.
Gomes, J.P., Lienhart, H., 2013. Fluid–structure interaction-induced oscillation of flexible structures in laminar and turbulent flows. Journal of Fluid Mechanics 715, 537–572.
Hémon, P., 2006. Vibrations des structures couplées avec le vent. Éditions de l'École Polytechnique, 82.
Hoerner, S.F., 1965. Fluid-Dynamic Drag. Published by the author, 25 (Chapter 3).
Howell, R.M., Lucey, A.D., Carpenter, P.W., Pitman, M.W., 2009. Interaction between a cantilevered-free flexible plate and ideal flow. Journal of Fluids and Structures 25, 544–566.
Huang, L., 1995. Flutter of cantilevered plates in axial flow. Journal of Fluids and Structures 9, 127–147.
Huang, L., Zhang, C., 2013. Modal analysis of cantilever plate flutter. Journal of Fluids and Structures 38, 273–289.
Huang, W.X., Sung, H.J., 2010. Three-dimensional simulation of flapping flag in a uniform flow. Journal of Fluid Mechanics 653, 301–336.
Kim, S., Huang, W.X., Sung, H.J., 2010. Constructive and destructive interaction modes between two tandem flexible flags in viscous flow. Journal of Fluid Mechanics 661, 511–521.
Landau, L.D., Lifshitz, E.M., 1986. Theory of Elasticity, third edition Butterworth Heinemann 38–104.
Lemaitre, C., Hémon, P., de Langre, E., 2005. Instability of a long ribbon hanging in axial flow. Journal of Fluids and Structures 20, 913–925.
Lokerson, D.T., 1968. Drag Device. United States Patent Office US 3374973.
Lord Rayleigh, 1878. On the instability of jets. Proceedings of the London Mathematical Society 10, 4–13.
Martin, A., 2006. Experimental Study of Drag from a Fluttering Flag. Master Thesis. Oklahoma State University.
Michelin, S., Llewellyn Smith, S.G., Glover, B.J., 2008. Vortex shedding model of a flapping flag. Journal of Fluid Mechanics 617, 1–10.
Michelin, S., Llewellyn Smith, S.G., 2010. Falling cards and flapping flags: understanding fluid-solid interactions using an unsteady point vortex model. Theoretical and Computational Fluid Dynamics 24, 195–200.
Michelin, S., Doaré, O., 2013. Energy harvesting efficiency of piezoelectric flags in axial flows. Journal of Fluid Mechanics 714, 489–504.
Moretti, P.M., 2003. Tension in fluttering flags. International Journal of Acoustics and Vibration 8 (4), 227–230.
Morris-Thomas, M.T., Steen, S., 2009. Experiments on the stability and drag of a flexible sheet under in-plane tension in uniform flow. Journal of Fluids and Structures 25, 815–830.
Païdoussis, M.P., 2004. Fluid–Structure Interactions: Slender Structures and Axial Flow, vol. 2. Elsevier.
Ristroph, L., Zhang, J., 2008. Anomalous hydrodynamic drafting of interacting flapping flags. Physical Review Letters 101, 194502.
Shelley, M., Vandenberghe, N., Zhang, J., 2005. Heavy flags undergo spontaneous oscillations in flowing water. Physical Review Letters 94, 094302.
Shelley, M.J., Zhang, J., 2011. Flapping and bending bodies interacting with fluid flows. Annual Review of Fluid Mechanics 43, 449–465.
Shukla, S., Govardhan, R.N., Arakeri, J.H., 2009. Flow over a cylinder with hinged-splitter plate. Journal of Fluids and Structures 25, 713–720.
Taneda, S., 1968. Waving motions of flags. Journal of the Physical Society of Japan 24 (2), 392–401.
Tang, D.M., Yamamoto, H., Dowell, E.H., 2003. Flutter and limit cycle oscillations of two-dimensional panels in three-dimensional axial flow. Journal of Fluids and Structures 17, 225–242.
Tang, L., Païdoussis, M.P., 2007. On the instability and the post-critical behaviour of two-dimensional cantilevered flexible plates in axial flow. Journal of Sound and Vibration 305, 97–115.
Tang, L., Païdoussis, M.P., Jiang, J., 2009. Cantilevered flexible plates in axial flow: energy transfer and the concept of flutter-mill. Journal of Sound and Vibration 326, 263–276.
Thoma, D., 1939a. Warum flattert die Fahne? Mitteilungen des Hydraulischen Instituts der Technischen Hochschule Münschen 9, 30–34.
Thoma, D., 1939b. Das schlenkernde Seil. Zeitschrift für Angewandte Mathematik und Mechanic 19 (5), 320–321.
Touzé, C., Bilbao, S., Cadot, O., 2012. Transition scenario to turbulence in thin vibrating plates. Journal of Sound and Vibration 331, 412–433.
Timoshenko, S.P., Gere, J.M., 1963. Theory of Elastic Stability, second edition McGraw-Hill.
Triantafyllou, G.S., 1992. Physical condition for absolute instability in inviscid hydroelastic coupling. Physics of Fluids 4 (3), 544–552.
Uno, M., 1973. Fluttering of flexible bodies. Journal of the Textile Machinery Society of Japan 26 (8), 73–79.
Watanabe, Y., Suzuki, S., Sugihara, M., Sueoka, Y., 2002a. An experimental study of paper flutter. Journal of Fluids and Structures 16 (4), 529–542.
Watanabe, Y., Isogai, K., Suzuki, S., Sugihara, M., 2002b. A theoretical study of paper flutter. Journal of Fluids and Structures 16 (4), 543–560.
Wilk, A., Skuta, M., 2009. Laboratory tests of the aerodynamic drag coefficient of the flag as a body with low stiffness. Task Quarterly 13 (1-2), 5–14.
Yadykin, Y., Tenetov, V., Levin, D., 2001. The flow-induced vibration of a flexible strip hanging vertically in a parallel flow. Part 1: temporal aeroelastic instability. Journal of Fluids and Structures 15, 1167–1185.
Yamaguchi, N., Yokota, K., Tsujimoto, Y., 2000a. Flutter limits and behaviors of a flexible thin sheet in high-speed flow—I: analytical method for prediction of the sheet behavior. Journal of Fluids Engineering, ASME 122, 65–73.
Yamaguchi, N., Sekiguchi, T., Yokota, K., Tsujimoto, Y., 2000b. Flutter limits and behaviors of a flexible thin sheet in high-speed flow—II: experimental results and predicted behaviors for low mass ratios. Journal of Fluids Engineering ASME 122, 74–83.
Zhang, J., Childress, S., Libchaber, A., Shelley, M., 2000. Flexible filaments in a flowing soap film as a model for one-dimensional flags in a two dimensional wind. Nature 408, 835–839.
Zhao, W., Païdoussis, M.P., Tang, L., Liu, M., Jiang, J., 2012. Theoretical and experimental investigations of the dynamics of cantilevered flexible plates subjected to axial flow. Journal of Sound and Vibration 331, 575–587.
Zhu, L., 2009. Interaction of two tandem deformable bodies in a viscous incompressible flow. Journal of Fluid Mechanics 635, 455–475.